JOURNAL OF MECHANICAL ENGINEERING AND SCIENCES (JMES)
ISSN: 2289-4659 e-ISSN: 2231-8380
VOL. 15, ISSUE 2, 7964 – 7982
DOI: https://doi.org/10.15282/jmes.15.2.2021.03.0628

ORIGINAL ARTICLE

CFD analysis of unsteady and anisotropic turbulent flow in a circular-sectioned 90° bend pipe with and without ribs: A comparative computational study

R. Chiremsel[1,*], A. Fourar[1], F. Massouh[2] and Z. Chiremsel[3]

[1] Department of Hydraulics, University of Batna 2, Research Laboratory in Applied Hydraulics, Constantine road N°53 Fesdis, Batna 05078, Algeria
Phone: +21333230202; Fax: +21333230222.
[2] National Higher School of Arts and Crafts (ParisTech; ENSAM), Laboratory of Fluid Mechanics 75013, France
[3] Safety Department, University of Batna2, IHSI-LRPI, Constantine road N°53.Fesdis, Batna 05078, Algeria

ABSTRACT – The Reynolds–averaged Navier–Stokes (RANS) equations were solved along with Reynolds stress model (RSM), to study the fully-developed unsteady and anisotropic single-phase turbulent flow in 90° bend pipe with circular cross-section. Two flow configurations are considered the first is without ribs and the second is with ribs attached to solid walls. The number of ribs is 14 ribs regularly placed along the straight pipe. The pitch ratios is 40 and the rib height e (mm) is 10% of the pipe diameter. Both bends have a curvature radius ratio, of 2.0. The solutions of these flows were obtained using the commercial CFD software Fluent at a Dean number range from 5000 to 40000. In order to validate the turbulence model, numerical simulations were compared with the existing experimental data. The results are found in good agreement with the literature data. After validation of the numerical strategy, the axial velocity distribution and the anisotropy of the Reynolds stresses at several downstream longitudinal locations were obtained in order to investigate the hydrodynamic developments of the analyzed flow. The results show that in the ribbed bend pipe, the maximum velocity value is approximately 47% higher than the corresponding upstream value but it is 9% higher in the case of the bend pipe without ribs. It was also found for both cases that the distribution of the mean axial velocity depends faintly on the Dean number. Finally, it can be seen that the analyzed flow in the bend pipe without ribs appears more anisotropic than in bend pipe with ribs.

ARTICLE HISTORY
Received: 20th July 2020
Revised: 27th Oct 2020
Accepted: 15th Dec 2020

KEYWORDS
RSM;
unsteady flow;
anisotropy function;
Dean number;
invariant anisotropy map

INTRODUCTION

Turbulent flows are common physical phenomena, which are very numerous in industrial and natural environments. They are the physical counterpart of the nonlinearity of the Navier-Stokes nonlinear differential equation, which is one of the most important in all physics arising from the fundamental principle of Newton's dynamics associated with the forces applied to a fluid in motion. Despite all the astounding and exceptional observations made by scientists and the existence of credible mathematical models faithfully reflecting turbulence, the latter remains so complex that it is almost impossible for physicists to make a clear statement on the matter. Turbulent flows occur in the fields of industry, fluid engineering, which seek to make good use of turbulence in order to improve mixing processes, prediction, and control of noise due to pressure fluctuations, improve heat exchange and mass transfers, and determine the hydraulic performance of equipment.

A study of turbulent, unsteady and anisotropic flows in 90° bend pipes is of great practical importance where anisotropy plays a role in the production of turbulent energy. Almost all bend pipes are presented in 90° devices and equipment incorporating fluids and flows such as the pulling pipe of hydraulic turbines and centrifugal pumps, energy production systems, transport lines, as well as in the human body, such as blood circulation in vessels and air in the respiratory tract [1, 2]. The flow in such geometries is complex and consists of a primary flow in the axial direction and a secondary flow (which consists of longitudinal vortices) generated as a result of an imbalance between the centrifugal force and the pressure gradient in the radial direction of curvature. This makes the precise numerical simulation of the flow difficult, in particular for turbulent, unsteady and anisotropic flows with high Reynolds number where it is extremely interesting to have knowledge on the expected anisotropy in the flow field [3]. Modeling the anisotropy of Reynolds stress tensor is the most important and delicate element of the Reynolds stress model, where knowledge of the deviation from isotropy is essential.

For this reason, the numerical simulation of the unsteady turbulent flows presenting an anisotropy between the turbulent normal stresses and the secondary flows induced by the ribs drawn up across the 90° bend of circular section to explore their influence on the disturbance of the flow arouses great scientific interest in the understanding and modeling of the various unsteady phenomena and a certain application interest, notably in the industrial field and has received much greater attention than suggests that the small amount devoted to it in specific works.

*CORRESPONDING AUTHOR | R. Chiremsel | ra24inf81@gmail.com

Several researchers have studied turbulent flows in bend pipes using theoretical, experimental and numerical methods. Ito [4] experimented with fully developed turbulent flow in a series of curved pipes, each with a different radius of curvature, Rc. He produced an experimental semi-empirical formula to calculate the frictional factor in smooth curved pipes. Lyne [5] initiated the theoretical study of unsteady flows in curved pipes, did the first experiment to confirm his theoretical findings. However, the experimental structure in his work was over simplified, and because of the small thickness of the Stokes layer, he could detect only the secondary motion in the interior tube region. Munson [6] investigated the unsteady flow caused by an oscillating axial pressure gradient in a curved pipe and determined the secondary velocity at the center of the pipe by recording the time for a spot of neutrally buoyant dye to travel a specified distance. Humphrey et al. [7] investigated the steady, incompressible, isothermal, developing flow in a square-section curved duct with smooth walls. The longitudinal and radial components of mean velocity and corresponding components of the Reynolds stress tensor were measured with a laser-Doppler anemometer along with the secondary mean velocities, driven mainly by the pressure field. Humphrey et al. [7] and Taylor et al. [8] measured the velocities of water and wall-pressure of developing turbulent flow through a square-sectioned 90° bend with a 4.5 radius ratio (with a short upstream tangent), which is the magnitude of the mean curvature radius to the half hydraulic diameter of the bend, using laser doppler velocimetry (LDV). They found that the boundary layer thickness at the start of the bend is important to the flow development within the bend, the pressure-driven secondary flows were much stronger than the stress-driven secondary flows and they provided detailed results including Reynolds stresses. Enayet et al. [9] and Azzola et al. [10] used laser doppler velocimetry for the measurements of water turbulent flows in bends with a circular cross-section. Longitudinal mean, fluctuating velocities and turbulent intensity fields were measured in a 90° bend with a radius ratio of 5.58 at a Reynolds number of 43000 by Enayet et al. [9] and in a 180° bend with a radius ratio of 6.75 at Re of 57400 and 110000 by Azzola et al. [10]. Unfortunately, these data are limited only to the longitudinal direction. Bovendeerd et al. [11] measured the velocity fields in a 90° bend with curvature ratio Rc/D=3, at *Re*=700 using the Laser Doppler Velocimetry (LDV). They choose oil and kerosene as a working fluid in order to match the refractive index of fluid to that of bend material. They obtained the time-averaged axial and secondary flow velocities. Ohadi and Sparrow [12] studied the heat transfer in the straight pipe downstream of a bend. Ohadi et al. [13] measured the pressure distribution in the pipe downstream of the bend. For a 90° elbow with the hydrodynamically-developed flow at the inlet to the elbow, they found only small differences in pressure gradient and friction coefficient in the pipe downstream of the elbow up to X/D=20, compared to those corresponding to fully developed flow. Al-Rafai et al. [14] performed an experimental and numerical study of turbulent airflow in the downstream region of the circular pipe bends to investigate the influence of Rc/D on the flow. Anwer and So [15] characterize the secondary motions in the following way: a so-called Dean cell is found near the pipe wall at the inside of the bend. This cell is directly driven by the centrifugal force and is therefore always present. A second cell may form near the pipe center as a result of a local imbalance between the centrifugal force and the pressure gradient. Finally, a third cell can sometimes be found at the outside of the bend. Its formation is attributed to the anisotropy of the turbulent normal stresses and their gradients. The second cell is only present in developing flow and the third cell is only found in a flow with a rather high Dean number. Kim and Patel [16] using a five-hole pressure probe and two-sensor hot-wire probes measured mean velocities and Reynolds stresses for developing turbulent flow in a 90° curved duct of rectangular cross-section. Their data showed that within the bend there is an extensive region of two-dimensional boundary layers under strong stream-wise curvatures and attendant pressure gradients. Moreover, their results showed the development of the pressure-driven secondary motion in the corner region which eventually leads to the formation of a longitudinal vortex on the convex wall. Hilgenstock and Ernst [17] modeled 45°, 90°, and 135° bends. They compared two turbulence models, namely the standard k–ε and the renormalization group (RNG) k–ε models, to experimental data. The RNG k–ε model was found to agree well with the experimental data and predicted the velocity profiles more accurately than the standard k–ε model but at the expense of increased CPU time. Xiaofeng and Ted [18] simulated numerically flows in curved tubes using a third party software package, FIDAP. The purpose of the work was to investigate the axial and secondary motions of developing flows. Kim et al. [19] compared the standard k–ε, RNG k–ε, realizable k–ε, RSM, and Spalart–Allmaras turbulence models in a range of complex flow situations. They showed that a second-order discretization scheme should be used for complex flows and that the wall functions provided an effective means of modeling the near-wall regions in wall-bounded flows. The RSM gave the best predictions, as the three k–ε-based models over-predicted the pressure recovery. Kim et al. [19] concluded that further studies were needed to understand the strengths and weaknesses of turbulence models in complex flows involving pressure gradient, streamline curvature, and separation. Sudo et al. [20] investigated experimentally the turbulent flow in a circular-sectioned 90° bend. The longitudinal, circumferential and radial components of mean and fluctuating velocities and the Reynolds stresses in the pipe cross-section at several longitudinal stations were obtained. They found that the curvature has a considerable impact on the pressure and velocity distributions. Kumar et al. [21] also conducted experimental studies in rough 90° bends of different radius ratio for single-phase flow and established that bend loss coefficient is minimum for a bend having radius ratio of 5.6 and also re-established that the flow disturbances caused by the bend persist up to 40–50 pipe diameters downstream of the bend and no significant disturbance is seen upstream of the bend. Hüttl and Friedrich [22] observed that the turbulent fluctuations in the curved pipe are drastically reduced compared to flow in a straight configuration and also provided a useful database, albeit at low Reynolds number, for flow modeling for a variety of configurations, including data for few selected terms of the Reynolds stresses. Kawamura et al. [23] measured the velocity field and turbulence intensity field in a 90° elbow with Rc/D=0.55, 1 and 2 at the $Re=5\times10^4$ and 5×10^5 using LDV measurement. They focused on the turbulent intensity and the characteristics of the power spectrum of the turbulent intensity. They gave the important findings that the normalized power spectrum of the turbulent intensity was not affected

by the Reynolds number. Though the separation occurred in the case of Rc/D=0.55 and 1, the unsteady flow structure formed by the separation and the secondary flow was not mentioned in detail. Chang and Lee [24] conducted experiments using the two-dimensional particle image velocimetry technique (PIV) with 21°C water as the fluid. Time-averaged velocity distribution and turbulence intensity of the swirl flow generated by a tangential inlet were obtained for a 90°bent tube for *Re*=10000, 15000, 20000 and 25000. Spedding et al. [25] measured the pressure drop in curved pipes and elbow bends for both laminar and turbulent single-phase flow and developed empirical correlations. The transitional Reynolds number for curved pipes of large bends was also determined using empirical relation. Pruvost et al. [26] investigated the fluid flow in the 90° and 180°bend with a small curvature ratio (Rc/D=0.25) using different turbulence models and wall equations. The results showed that the relation between swirl motion and Dean motion is complicated and swirl motion has an inhibitory effect against Dean motion. Raisee et al. [27] investigated numerically developing turbulent flow through two different 90°curved ducts: a square duct and a rectangular duct. The low-*Re* models of turbulence are employed. The main objectives of their study are to examine how curvature alters flow development in the curved ducts and to explore the predictive capabilities of a recently modified variant of the cubic non-linear *k-ε* model, relative to those of the linear low-*Re k-ε* model, in predicting flow characteristics in curved ducts. According to the conclusions, both models could show a satisfactory prediction of the mean flow filed. The nonlinear *k-ε* model has better performance for turbulence field, pressure and friction coefficients, but it is not accurate for the prediction of flow recovery after the bend exit. Crawford et al. [28] investigated numerically the pressure drop for turbulent flow in 90° elbow bends. Shiraishi et al. [29] and Shiraishi et al. [30] measured the pressure fluctuation and observed the flow regime in the pipe with elbow with Rc/D=1 up to the $Re=8.0\times10^6$. Although they concluded that the fluctuating pressure was generated by the movement of the boundary of flow separation and reattachment region, their data of axial velocity profile in the elbow measured by LDV was limited at several positions and not enough to understand clearly the complex and unsteady flow field around the flow separation region. Mojtaba et al. [31] used the PIV technique allows reliable measurement of the velocity vectors of the secondary motion in a developing laminar pulsating flow through a curved pipe. Analysis of the vorticity and strain variations during an oscillation period then identifies favorable pulsating conditions that enhance mixing. Ono et al. [32] investigated using water experiments in elbows the mechanism of flow fluctuation induced by the interaction between the flow separation and secondary flow due to the elbow curvature. The elbow curvature ratio was chosen as an experimental parameter in order to change the intensity of the secondary flow induced by the centrifugal force. The time-series of velocity fields in the elbows were measured using a high-speed Particle Image Velocimetry (PIV). Noorani et al. [33] investigated the evolution of selected characteristics of the turbulent flow in straight to bent pipes over a limited range of Reynolds numbers and curvatures. Min and Zhiguo [34] provided high-resolution velocity maps of the primary and secondary flow upstream and downstream of a 90° bend pipe. The flow field parameters were obtained using numerical methods at *Re*=10000. One of the particular areas of interest is the behavior of the vorticity, turbulent structure, specifically the Dean vortex and swirling flow upstream and downstream of a 90° bend pipe. Niu and Dou [35] used the energy gradient theory to analyze numerical simulation of the flow in a 90° bend with a square cross-section. This study shows that the occurrence of instability is closely related to the evolution of the energy gradient function. Hellström et al. [36] investigated experimentally the secondary flow structures downstream of a 90° bend to try and resolve some of these ambiguities with Reynolds numbers between 2×10^4 and 1.15×10^5. Specifically, they investigated the nature of the swirl switching mode and its relationship to the Dean motions, using snapshot proper orthogonal decomposition (POD). Jongtae et al. [37] performed experimental and numerical studies on turbulent pipe flow after 90° elbows and to characterize the secondary flows induced by the 90° elbows including the dissipation characteristics. Dutta and Nandi [38] studied the pressure drop characteristics of single-phase turbulent flow downstream of the elbow for high Reynolds number (*Re*= 1×10^5 to 10×10^5) and for different curvature ratio (Rc/D=1 to 5) using *k-ε* RNG turbulence model with standard wall function. Yan et al. [39] predicted by numerical simulation the fluid flows through a curved pipe for Rc/D>0.5. Flow behaviors such as, secondary flow, boundary layer separation and the oscillatory flow are illustrated and studied. Furthermore, the variation of flow characteristics, such as the turbulence intensity and the secondary flow intensity is estimated for a given flow condition. Röhrig et al. [40] compared RANS and LES simulations to PIV data on cross-sections downstream of the elbow, validating the LES velocity and pressure field calculations. Dutta et al. [41] presented the simulation of the flow pattern in 90° pipe bends with different curvature ratios with different Reynolds numbers. The details of the flow pattern throughout the bend were studied. The variations of velocity profiles with curvature ratio and Reynolds number were studied. The dependency of swirl intensity on a wide range of curvature ratio and Reynolds number are unique features. Wang et al. [42] employed Direct Numerical Simulation and studied a turbulent pipe flow with 90° bends.

In this study, we examine the development of unsteady and anisotropic turbulent flow while considering a circular-sectioned 90° bend pipe with and without ribs. This geometry is of particular interest since it has been the subject of multiple experimental campaigns and numerical studies in recent years which have made it possible to advance in the understanding of the flow topology involved in this hydraulic installation.

To select a suitable turbulence model for the numerical simulation of an unsteady and anisotropic turbulent flow in a bend pipe, the validation of the numerical results of the turbulence model is very important. The experiments carried out by Sudo et al. [20] on turbulent flows in 90° bend pipe are used to validate the chosen turbulence model. With this in mind, the RSM turbulence model was selected to evaluate accurately the characteristics of the analyzed flow at the outlet of the bends, but its application to turbulent flows in three-dimensional complex engineering problems requires tremendous computational resources. Simulations are carried out to choose the mesh which gives the best compromise between the precision of the results and calculation time.

Useful tools for quantifying the degree of anisotropy in turbulent flows are anisotropy maps. These maps represent a domain in which all the invariants of the realizable Reynolds stresses must be found. In this work, an invariant anisotropy map (AIM) which is a representation proposed by Lumley and Newman [43] is used.

Considering the above, the objectives of this work are, therefore, on the one hand, to study the effect of the 90° bend pipe with and without ribs on the degree of anisotropy of turbulence to improve our knowledge and on hydraulic performance inherent phenomena (velocity distributions, departures from isotropy) at the exit of the curvature, while carrying out a comparative study between these two geometric models and on the other hand to assess the capacity of the RANS turbulence modeling approach and the RSM turbulence model to faithfully reproduce the flow in these systems as part of the numerical simulation of an unsteady and anisotropic turbulent flow by considering a total of four flow conditions. These flow conditions are selected to study the effect of the increase in the Dean number on the behavior of the type of flow studied.

DESCRIPTION OF THE PHYSICAL PROBLEM

The problem that is considered here is the fluid flow characteristics through two circular-sectioned 90° bending pipes having a diameter D=50 (mm) and curvature ratio (Rc/D)=2. For both cases, the lengths of the upstream and downstream sections are 15D and 10D respectively. The first bend pipe is considered without ribs and the second is with square ribs. The number of which is 14 ribs regularly placed along the straight pipe. The pitch ratios Pt/e=40 where Pt-e=195 (mm) is the distance between two successive ribs and e (mm) is the rib height. The rib height e is 10% of the pipe diameter (e/D=0.1). It is defined that the axial direction downstream the bend is x-coordinate, the direction from the inner core to the outer core of the bend is y-coordinate and the perpendicular direction to x and y is z-coordinate. The geometry of the flow field for both cases is shown in Figure 1.

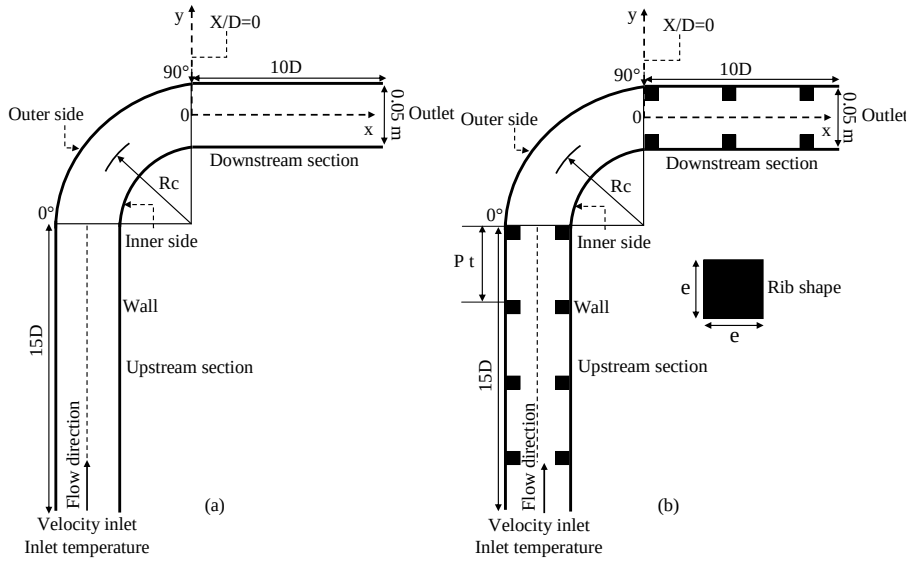

Figure 1. Schematic representation of bends investigated: (a) 90° bend pipe without ribs and, (b) 90° bend pipe with ribs

GOVERNING CONSERVATION EQUATIONS OF TURBULENT FLOW

Three-dimensional governing equations under consideration of the RANS simulation are solved using the finite volume method [44]. The second-order upwind scheme was implemented for the solution of momentum terms. The SIMPLE algorithm is used for pressure-velocity coupling [45].

Considering an incompressible and Newtonian fluid, three-dimensional continuity and momentum equations used in this numerical analysis in cartesian tensor notation can be written respectively as in Eq. (1) and (2).

$$\frac{\partial U_i}{\partial x_i} = 0 \tag{1}$$

$$\frac{\partial U_i}{\partial t} + \frac{\partial}{\partial x_j} U_i U_j = -\frac{1}{\rho}\frac{\partial P}{\partial x_i} + \nu \frac{\partial^2 U_i}{\partial x_j^2} - \frac{\partial}{\partial x_j}\left(\overline{u_i' u_j'}\right) \tag{2}$$

where U_i (m/s) is the axial mean velocity, P (Pa) the mean pressure, x_i (m) the coordinate vector, t (s) the time, ρ (kg/m^3) the density, ν (m^2/s) the kinematic viscosity while $\overline{u_i' u_j'}$ (m^2/s^2) denotes the Reynolds stress tensor.

The Reynolds averaging equations are preceded by a decomposition of the instantaneous values of velocity and pressure into a mean and a turbulent fluctuating quantity [46] which are given respectively in Eq. (3) and (4).

$$u_i = U_i + u_i^{'} \tag{3}$$

where u_i (m/s) is the instantaneous velocity and $u_i^{'}$ (m/s) denotes the fluctuating velocity.

$$p_i = P_i + p_i^{'} \tag{4}$$

where p_i (Pa) is the instantaneous pressure, P_i (Pa) the mean pressure and $p_i^{'}$ (Pa) the fluctuating pressure.

The new term $\overline{u_i' u_j'}$ that appears in the RANS equation Eq. (2) somehow represents the average of the pulse transfer rate due to turbulence. In three dimensions, it is described by Eq. (5).

$$\overline{u_i^{'} u_j^{'}} = \begin{bmatrix} \overline{u^{'}u^{'}} & \overline{u^{'}v^{'}} & \overline{u^{'}w^{'}} \\ \overline{u^{'}v^{'}} & \overline{v^{'}v^{'}} & \overline{v^{'}w^{'}} \\ \overline{u^{'}w^{'}} & \overline{v^{'}w^{'}} & \overline{w^{'}w^{'}} \end{bmatrix} \tag{5}$$

This term comes from the non-linearity of the convection term of the Navier-Stokes equations. It comes with the addition of a number of additional unknowns. The tensor being symmetrical, the number of additional unknowns is 6 for three-dimensional problems. This addition of unknowns without adding equations leads to the problem known as the closure problem. It will therefore naturally be necessary to find new equations to solve the system.

Turbulence Modelling Equations

In order to close the RANS equations, a model of turbulence must be provided. The transport equations include a number of unknowns. The aim of turbulence modeling is to treat these unknowns in terms of the physically known properties. It is now accepted that, without modification, conventional turbulent viscosity models are incapable faithfully reproducing the behavior of secondary flows, whereas the Reynolds stress model has proved capable of predicting such flows. One of the main characteristics of second-order closings lies in the possibility of representing the different mechanisms that govern the evolution of double correlations [47].

In this paper, the Reynolds stress model (RSM) is proposed, the latter proved to be able to predict the anisotropy of turbulent flows [48]. RSM is theoretically more adapted when turbulence is found to be anisotropic, as in bend flows [49]. This RSM model is extremely complicated to solve the three-dimensional equations, where the differential transport equations are solved for each Reynolds stress component which requires more effort and time to simulate the flow. These equations include some terms that are exact and some that must be modeled [50]. The modeled terms require a variety of ad hoc wall damping functions and the numerical values of the coefficients are chosen based on empiricism [51].The exact transport equations for the transport of the Reynolds stresses, $\overline{u_i' u_j'}$ may be written using following Eq. (6).

$$\frac{\partial \overline{u_i^{'} u_j^{'}}}{\partial t} + U_k \frac{\partial \overline{u_i^{'} u_j^{'}}}{\partial x_k} = \nu \frac{\partial^2 \overline{u_i^{'} u_j^{'}}}{\partial x_k \partial x_k} - \frac{\partial \overline{u_i^{'} u_j^{'} u_k^{'}}}{\partial x_k} - \frac{1}{\rho} \overline{u_i^{'} \frac{\partial p^{'}}{\partial x_j}} - \frac{1}{\rho} \overline{u_j^{'} \frac{\partial p^{'}}{\partial x_i}} - \overline{u_i^{'} u_k^{'}} \frac{\partial U_j}{\partial x_k} - \overline{u_j^{'} u_k^{'}} \frac{\partial U_i}{\partial x_k} - 2\nu \overline{\frac{\partial u_i^{'}}{\partial x_k} \frac{\partial u_j^{'}}{\partial x_k}} \tag{6}$$

where $\overline{u_i' u_j' u_k'}$ (m^3/s^3) is the triple correlations of fluctuating velocities.

Equation (6) can be written as the following Eq. (7).

$$\frac{D\overline{u_i' u_j'}}{Dt} = P_{ij} - \varepsilon_{ij} + \emptyset_{ij} + D_{ij}^{T} + D_{ij}^{\nu} \tag{7}$$

The turbulent production, convection, viscous dissipation, velocity-fluctuating pressure correlation, turbulent diffusive transport and molecular diffusion are defined using respectively following Eq. (8), (9), (10), (11), (12) and (13).

$$P_{ij} = -\overline{u_i' u_k'} \frac{\partial U_j}{\partial x_k} - \overline{u_j' u_k'} \frac{\partial U_i}{\partial x_k} \tag{8}$$

$$C_{ij} = U_k \frac{\partial \overline{u`_i u`_j}}{\partial x_k} \tag{9}$$

$$\varepsilon_{ij} = 2\nu \overline{\frac{\partial u_i'}{\partial x_k} \frac{\partial u_j'}{\partial x_k}} \tag{10}$$

$$\Phi_{ij} = -\frac{1}{\rho}\overline{u_i'\frac{\partial p'}{\partial x_j}} - \frac{1}{\rho}\overline{u_j'\frac{\partial p'}{\partial x_i}} \tag{11}$$

$$D_{ij}^T = -\frac{\partial \overline{u_i'u_j'u_k'}}{\partial x_k} \tag{12}$$

$$D_{ij}^\nu = \nu\frac{\partial^2 \overline{u_i'u_j'}}{\partial x_k \partial x_k} \tag{13}$$

The terms, C_{ij}, D_{ij}^ν and P_{ij} can be preserved in their exact form, no modeling is necessary. However the terms D_{ij}^T, Φ_{ij} and ε_{ij} require modeling that provides mathematical relationships to close the system. For the ε-based RSM, D_{ij}^T can be modeled as given by Eq. (14) [52].

$$D_{ij}^T = \frac{\partial}{\partial x_k}\left(\frac{\mu_t}{\sigma_k}\frac{\partial \overline{u_i'u_j'}}{\partial x_k}\right) \tag{14}$$

where σ_k is an empirical constant and μ_t is the turbulent viscosity (kg/(m.s)) which is computed by Eq. (15).

$$\mu_t = \rho C_\mu \frac{k^2}{\varepsilon} \tag{15}$$

k (m^2/s^2) is the turbulent kinetic energy, ε (m^2/s^3) the turbulence dissipation rate and C_μ is an empirical constant.

By default in ANSYS Fluent, the pressure-strain term, Φ_{ij} is modeled according to the proposals by Gibson and Launder [53], Fu et al. [54] and Launder [48]. The classical approach to modeling Φ_{ij} uses the following decomposition which is given in Eq. (16).

$$\Phi_{ij} = \Phi_{ij,1} + \Phi_{ij,2} + \Phi_{ij,w} \tag{16}$$

$\Phi_{ij,1}$ is the slow pressure-strain term, also known as the return-to-isotropy term, $\Phi_{ij,2}$ is called the rapid pressure-strain term, and $\Phi_{ij,w}$ is the wall-reflection term. The slow pressure-strain term $\Phi_{ij,1}$ is modeled as in Eq. (17).

$$\Phi_{ij,1} = -C_1\rho\frac{\varepsilon}{k}\left(\overline{u_i'u_j'} - \frac{2}{3}\delta_{ij}k\right) \tag{17}$$

The rapid pressure-strain term $\Phi_{ij,2}$ is modeled as in Eq. (18).

$$\Phi_{ij,2} = -C_2\left(\left(P_{ij} - C_{ij}\right) - \frac{1}{3}\delta_{ij}(P_{kk} - C_{kk})\right) \tag{18}$$

where δ_{ij} is the Kronecker symbol, C_1 and C_2 are the empirical constants.

The wall-reflection term $\Phi_{ij,w}$ is responsible for the redistribution of normal stresses near the wall. It tends to damp the normal stress perpendicular to the wall while enhancing the stresses parallel to the wall. This term is modeled using the Eq. (19).

$$\begin{aligned}\Phi_{ij,w} \;=\; & C_1'\frac{\varepsilon}{k}\left(\overline{u_k'u_m'}n_k n_m\delta_{ij} - \frac{3}{2}\overline{u_i'u_k'}n_j n_k - \frac{3}{2}\overline{u_j'u_k'}n_i n_k\right)\frac{C_\mu^{3/4}k^{3/2}}{\varepsilon d\kappa} \\ & + C_2'\left(\Phi_{km,2}n_k n_m\delta_{ij} - \frac{3}{2}\Phi_{ik,2}n_j n_k - \frac{3}{2}\Phi_{jk,2}n_i n_k\right)\frac{C_\mu^{3/4}k^{3/2}}{\varepsilon d\kappa}\end{aligned} \tag{19}$$

where n_k is the unit vector normal to the wall, d is the normal distance to the wall, κ the von Kármán constant while C_1' and C_2' denote an empirical constants.

For Reynolds stress models based on the ε-equation, the dissipation tensor ε_{ij} is modeled as shown in Eq. (20).

$$\varepsilon_{ij} = \frac{2}{3}\delta_{ij}(\rho\varepsilon + Y_M) \tag{20}$$

where Y_M is an additional dilatation dissipation term according to the model of Sarkar and Balakrishnan [55].

$$Y_M = 2\rho\varepsilon M_t^2 \tag{21}$$

From Eq. (21), the turbulent Mach number M_t is defined as:

$$M_t = \sqrt{\frac{k}{a^2}} \tag{22}$$

where in Eq. (22), a (m/s) is the speed of sound.

The scalar dissipation rate, ε, is computed with a model transport equation similar to that used in the standard k-ε model, it is found by solving its transport equation that can be denoted as in Eq. (23).

$$\frac{\partial}{\partial t}(\rho\varepsilon) + \frac{\partial}{\partial x_i}(\rho\varepsilon u_i) = \frac{\partial}{\partial x_j}\left[\left(\mu + \frac{\mu_t}{\sigma_\varepsilon}\right)\frac{\partial \varepsilon}{\partial x_j}\right] + C_{\varepsilon 1}\frac{P_{ii}}{2}\frac{\varepsilon}{k} - C_{\varepsilon 2}\rho\frac{\varepsilon^2}{k} \tag{23}$$

where μ (kg/(m.s)) is the dynamic viscosity while σ_ε, $C_{\varepsilon 1}$ and $C_{\varepsilon 2}$ denote an empirical constants.

The constant values for the Reynolds stress model are given in Table 1.

Table 1. Empirical constants for the RSM model

C_μ	σ_k	C_1	C_2	C_1'	C_2'	κ	σ_ε	$C_{\varepsilon 1}$	$C_{\varepsilon 2}$
0.09	0.82	1.8	0.6	0.5	0.3	0.4187	1.0	1.44	1.92

MESH GENERATION AND GRID INDEPENDENCE STUDY

In this study, for both geometries, 3D structured hexahedral meshes with inflation near the walls are used due to its capabilities in providing a high-quality solution with fewer numbers of cells, higher accuracy and reduce CFD computational effort [56, 57]. Using the sizing functions, a high adaptive mesh density was maintained in the bend and regions close to the wall and ribs where the mesh is stretched from the solid wall toward the centerline to gain a higher resolution near the wall, where better resolution is needed [58]. The value of non–dimensional distance from the wall (y+) is controlled using a wall treatment function. The wall treatment used for all of the computations reported is the standard wall function approach. The grid generation is a key issue in flow simulation that governs the stability, the accuracy of the predictions and the time of CFD numerical computation. A very fine grid is computationally more expensive and is necessary to ensure reasonable resolution of the mesh [59, 60]. The appropriate quality and quantity of grids are very important. In this study, five three-dimensional meshes are generated by using ANSYS ICEM to optimize the mesh convergence by study the effects of grid numbers on the stability of numerical results and ensure that the solution was independent of the mesh. They are summarized in Table 2. The convergence criterion used for these calculations is 10^{-5} for continuity and 10^{-4} for the other flow equations.

Table 2. Grid convergence study

Mesh	Number of nodes	Number of elements
Mesh1	602745	140070
Mesh2	1605075	390264
Mesh3	4019697	981834
Mesh4	6234372	1534929
Mesh5	12241833	3018520

In Figure 2 the mean axial velocity profile at X/D=0 is used in a grid independence test where X (m) is defined as the position on the longitudinal axis, R (mm) is the radius of the pipe, r (mm) denotes the radial distance and the Dean number is De=3×10^4. Based on the results, it appears that the distribution of the mean axial velocity U_x normalized by the inlet velocity u_{in} (U_x/u_{in}) obtained for the mesh-5 does match with the profile obtained for the mesh-4. It can be clearly observed that the relative deviation of axial velocity between mesh-4 and mesh-5 is only 0.078%. Therefore, it was concluded that the mesh-4 consists of 1534929 elements and 6234372 nodes ensures a grid-independent solution and this mesh is used for all analyses in this study.

Referring to Table 3, the mesh quality is excellent, where the metrics skewness and aspect ratio are equal to 0.25 and 0.52 respectively. The following table lists the range of skewness values and the corresponding cell quality.

Table 3. Classification of the mesh quality metrics based on skewness [61].

0-0.25	0.25-0.50	0.50-0.75	0.75-0.9	0.9-<1	1
Excellent	Good	Fair	Poor	Bad(sliver)	Degenerate

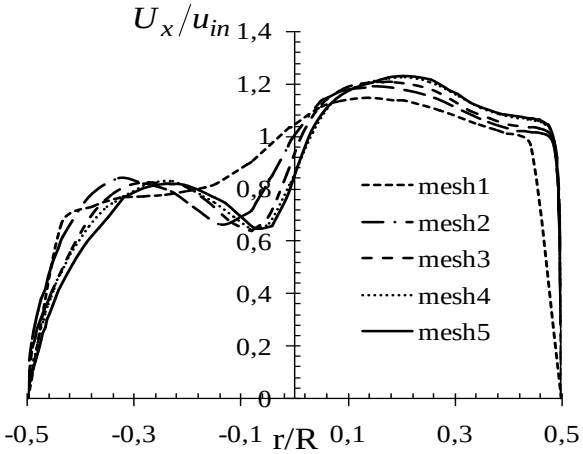

Figure 2. Normalized mean axial velocity distribution for different structured meshes

Validation of Model

After establishing grid independence, the selection of an appropriate turbulence model for the numerical simulation of an unsteady and anisotropic turbulent flow in a bend pipe is very important. For it, our turbulent model and simulation setup are first validated against the existing experimental data with air as the working fluid [20] where the measurements of velocities were performed at a Dean number of 3×10^4. The mean axial velocity profile normalized with inlet velocity along the symmetry line at different sections downstream the bend shows very good agreement with the experimental measurements currently available (see Figure 3). The four evolutions are perfectly superimposed and the observed difference between the different results is barely remarkable where for X/D=0, X/D=0.5, X/D=1 and X/D=2, the maximum errors of mean axial velocity differences range between 5% and 6% where a similar behavior is observed with the published results however at X/D=5 the errors is around 14%. This translates that in the case of experimental data of Sudo et al. [20], the mean axial velocity profile is significantly altered and take the form of the fully-developed turbulent profile. However, in the present simulation, a further longitudinal distance is required for the flow to be fully developed turbulent. The estimates of errors are summarized in the following table.

Table 4. Measurement errors (%)

X/D	Error (%)
0	5.34
0.5	5.75
1	5.95
2	5.54
5	13.66

In view of the above, the trends for the mean axial velocity profiles are well captured properly and accurately by the RSM model which appears superior in predicting the axial velocity peak; this is due that the RSM model was formulated by involving the strong anisotropic turbulent flows. However, the effort of obtaining the converged solution using RSM model is not easy.

From the Figure 3, it was found that the use of the Reynolds stress model (RSM) presents a very sufficient approximation with the published results; therefore, this mesh generation and simulation configuration procedure was used for the rest of our study by adopting the RSM model as the turbulence model.

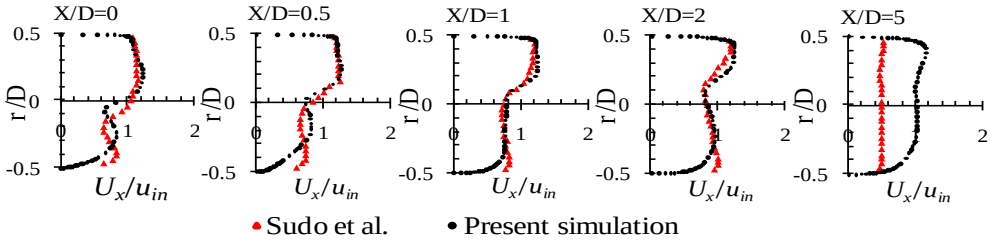

Figure 3. Comparisons of the non-dimensional mean axial velocity profiles with experimental data of Sudo et al. [20], along the symmetry line, at different sections downstream of the bend

BOUNDARY CONDITIONS AND NUMERICAL DETAILS

The resolution of the nonlinear governing equations presented above, is done by the use of the defined boundary conditions which are described in Figure 1. A total of four flow conditions, as shown in Table 5, are studied in this study. Inlet boundary conditions applied in entry are defined in terms of velocity, temperature, turbulent kinetic energy and specific dissipation rate. The velocity at the inlet was calculated based on the Reynolds number referred to the pipe diameter and entrance flow conditions. The fluid inlet temperature was fixed at 293k. The values of the turbulent kinetic energy and its specific dissipation rate are calculated from the inlet turbulence intensity and pipe diameter using Eq. (24) and (25) respectively.

$$k_{in} = 1.5\left(I{u_{in}}^2\right) \tag{24}$$

$$\varepsilon_{in} = (C_\mu k^{1.5})/0.3\mathrm{D} \tag{25}$$

The turbulence intensity is defined by Eq. (26).

$$I = 0.16Re^{-0.125} \tag{26}$$

At the pipe wall no slip boundary conditions for the velocity has been applied and the wall was treated as stationary. The outlet was given as outflow and the working fluid (water) was supposed to be incompressible with constant properties summarized in Table 6 where *cp* ($J.kg^{-1}.K^{-1}$) denotes the specific heat and k ($W.m^{-1}.k^{-1}$) is the thermal conductivity. The flow was assumed to be three-dimensional turbulent, unsteady and anisotropic.

In the analysis of flows through bend pipes the Dean number is used frequently. It is defined according to the following equation:

$$\mathrm{De} = Re\sqrt{\frac{\mathrm{D}}{2Rc}} \tag{27}$$

From Eq. (27), Rc (mm) is the radius of curvature and *Re* is the Reynolds number.

Table 5. List of flow conditions investigated in the current study

Flow conditions	*De*	u_{in}	k_{in}	ε_{in}	*I* (%)
Run 1	5000	0.200	0.0001500	1.102E-5	5
Run 2	10000	0.402	0.0005129	6.969E-5	4.60
Run 3	20000	0.804	0.0017514	4.399E-4	4.25
Run 4	40000	1.608	0.0058990	2.718E-3	3.90

Table 6. Thermophysical properties of the fluid at T=293k

ρ	*cp*	K	μ
998.21	4182	0.6024	0.001003

The second-order upwind scheme was implemented for the solution of momentum terms. The SIMPLE algorithm is used for pressure-velocity coupling. The time step size and the number of time steps used in current simulations

considering established flow conditions are summarized in Table 7. The Solutions of these flows were obtained using the commercial computational fluid dynamics (CFD) software Fluent at a Dean number ranging from 5000 to 40000. Analysis results at different locations downstream of the bend were used in this study.

Table 7. List of flow run calculations investigated in the current simulations

	Bend pipe without ribs		Bend pipe with ribs	
Flow conditions	Time step size	Number of time steps	Time step size	Number of time steps
Run 1	18.970E-4	3708	20.810E-4	3381
Run 2	9.438E-4	3708	10.353E-4	3381
Run 3	4.719E-4	3708	5.177E-4	3381
Run 4	2.359E-4	3708	2.588E-4	3381

ANISOTROPY TENSORS

To highlight the anisotropic character of the flow, it is often convenient to use the so-called anisotropy invariant maps (AIM) or Lumley triangles. To investigate and quantify the degree of anisotropy in turbulent flows, the technique proposed by Lumley and Newman [43], is based on the analysis of the anisotropy tensor a_{ij} which is the result of decomposing the Reynolds stress tensor into an anisotropic and an isotropic term as shown in Eq. (28) [43].

$$a_{ij} = \frac{\overline{u_i' u_j'}}{2k} - \frac{1}{3}\delta_{ij} \tag{28}$$

The turbulent kinetic energy can be therefore defined as in Eq. (29).

$$k = \frac{1}{2}\overline{u_i' u_j'} = \frac{1}{2}\left(\overline{u'^2} + \overline{v'^2} + \overline{w'^2}\right) \tag{29}$$

In matrix form, a_{ij} can be written as given in Eq. (30) below:

$$[a_{ij}] = \begin{bmatrix} a_{11} & a_{12} & a_{13} \\ a_{21} & a_{22} & a_{23} \\ a_{31} & a_{32} & a_{33} \end{bmatrix} \tag{30}$$

This tensor has three independent scalar invariants, which are described by Eq. (31) to (33) [43, 62].

$$\mathrm{I} = a_{ii} = 0 \tag{31}$$

where the invariant *I* is the trace of the anisotropy tensor a_{ij}, therefore it is identically zero.

$$\mathrm{II} = a_{ij}a_{ji} \tag{32}$$

$$\mathrm{III} = a_{ik}a_{kj}a_{ji} \tag{33}$$

The second invariant *II* represents the degree of anisotropy whereas *III* represents the nature (or topology) of the anisotropy. A plot of -*II* versus *III*, defines the anisotropy invariant map (AIM which defines the domain of validity of the tensor a_{ij} whose limits are represented by Eq. (34), (35) and (36).

$$9\mathrm{II} + 27\mathrm{III} + 1 = 0 \tag{34}$$

$$\mathrm{III} = 2\left(\frac{-\mathrm{II}}{3}\right)^{3/2} \tag{35}$$

$$\mathrm{III} = -2\left(\frac{-\mathrm{II}}{3}\right)^{3/2} \tag{36}$$

Therefore, anisotropy can be more clearly seen from these anisotropy maps. Characteristic states of turbulence are represented by the boundaries of this map as shown in Figure 4.

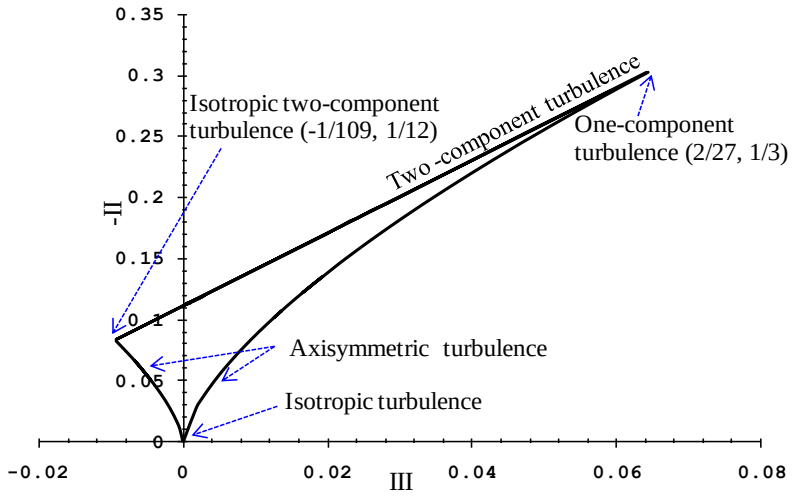

Figure 4. The anisotropy invariant map (AIM), showing admissible domain of anisotropy in invariant coordinates, *-II* vs *III* [43]

For the case of anisotropic turbulence we distinguish three states of anisotropy that occur within the bounds of the AIM. The upper limit of the AIM corresponds to two-component turbulence where one of the normal components of the Reynolds tensor is zero. The two curves correspond to the axisymmetric states, of type pancake-shaped ($III \leq 0$) in which one component is smaller than the other two components which are equal and of type cigar-shaped ($III \geq 0$) corresponding to a situation where one diagonal component of Reynolds stress tensor is larger than the other two equally distributed components. The origin of the graph (II=0, III= 0) corresponds to 3D isotropic turbulence, where $\overline{u'^2} = \overline{v'^2} = \overline{w'^2}$. The right corner point (2/27,1/3), characterizes one-component turbulence and the end of the left curve (-1/109,1/12), represents isotropic two-component turbulence.

To evaluate the flow anisotropy, Lumley [3] introduced another invariant function J which is defined by Eq. (37). This function is used to determine the linear distance to the isotropic state. In another way, it measures the difference between isotropic and two-component turbulence. Therefore for two-component turbulence, J is close to zero and J=1 for isotropic turbulence.

$$J = 9II + 27III + 1 \tag{37}$$

RESULTS AND DISCUSSION

The main objective of the current study is, on the one hand, the comparison of the hydrodynamic behavior of unsteady and anisotropic single-phase turbulent flow into 90° bend pipe without and with ribs through numerical simulation along the different positions downstream of the bend and on the other hand investigate how the ribs affect the three-dimensional unsteady and anisotropic turbulent flow and turbulence characteristics such as velocity distributions, anisotropy of the Reynolds stresses and anisotropy function.

The results are reported in terms of the normalized mean axial velocity, Reynolds stresses anisotropy and anisotropy function as a function of Dean number ranging from 5×10^3 to 40×10^3.

Mean Velocities

The distributions of mean axial velocity normalized by the inlet velocity u_{in} and its evolution with the increasing of downstream location and the Dean number are presented in Figure 5. The negative r (mm) values represent the inner core of the bend and the positive values represent the outer core. The data displayed are taken in the symmetry plane of the configuration according to the coordinate r which extends perpendicular to the centerline.

An examination of Figure 5 shows that for the two geometric models considered, the distribution of the mean axial velocity does not present any great difference between the different Dean numbers used, which means that there is a similarity in the structure of the analyzed flow after the elbow with the radius of curvature adopted if the Dean number is between 5000 and 40000. We deduce that for the bend pipe with a small curvature ratio (Rc/D≤2) the Dean number is found as a weak function.

For the case of bend without ribs Figure 5, we observe a significant shift of the peak velocity towards the outer wall just at the exit of the bend up to a distance X=2.5D. The velocity profile has an inflection point corresponding to a change in concavity causing a rate of increase in acceleration towards the outer wall of the pipe. This acceleration is due to the pressure gradients that develop at the entrance to the elbow due to the centrifugal force. The main characteristic of this

flow in this area is the appearance of camel back shapes in the distribution of velocity. These forms are the result of the loss of momentum.

By moving away from the bend and from X=5D, we see that the flow tends to regain its fully developed form, the velocity profile is approximately symmetrical (flattened form) and similar behavior has been observed.

From Figure 5 again, in the bend pipe with ribs, the fluid moves more quickly and the mean axial velocity has been accelerated at the central region of the pipe. The maximum velocity value is approximately 47% higher than the corresponding upstream value but it is 9% higher in the case of the bend pipe without ribs.

It is found that the fluid is somewhat displaced towards the exterior surface of the wall. Consequently, the flow tends to regain its fully developed form in the inner heart downstream the bend by slowing the effects thanks to the ribs placed upstream and downstream of the bend where the flattened form in the central part of the pipe is observed at X=D. The recovery of the profile seems to be caused by turbulent transport, which should be more important in the presence of ribs.

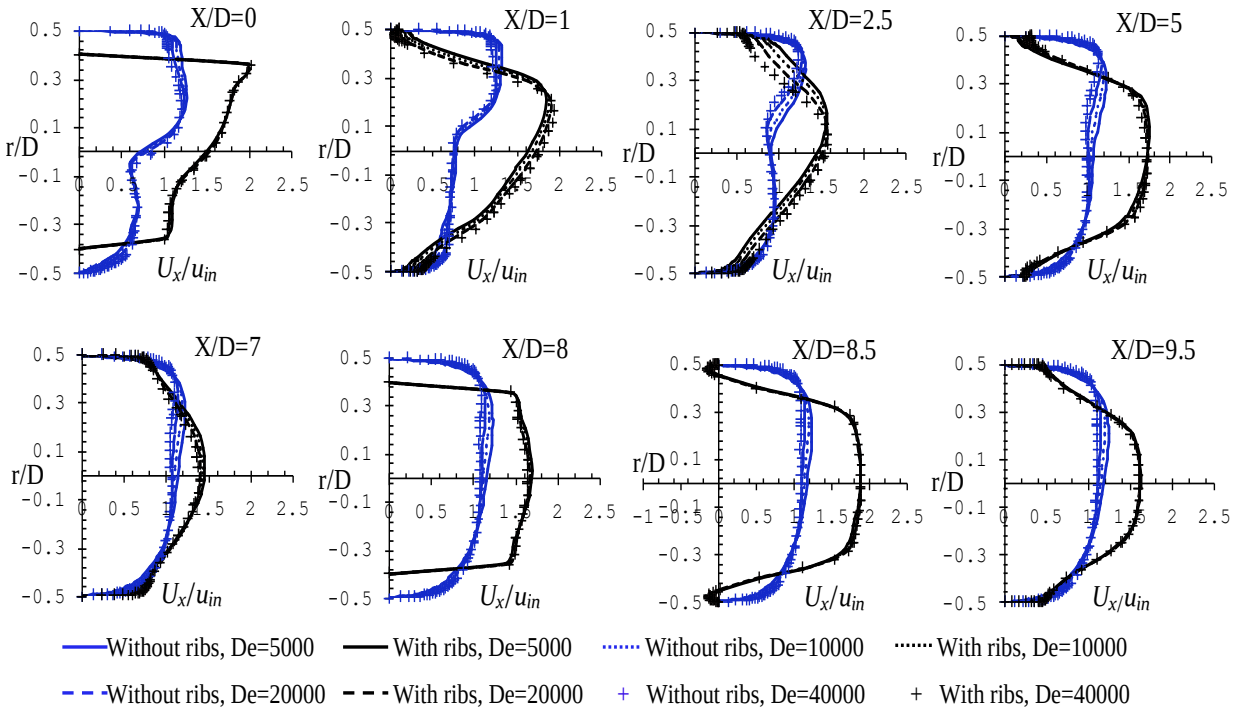

Figure 5. Comparison of normalized mean axial velocity profiles at different locations downstream the bends with and without ribs obtained with RSM model, *De*=5000, 10000, 20000 and 40000

We observed a secondary flow structure composed of two counter-rotating cells located downstream of the second rib at X=8.5D. These vortices appear to be induced near the inner and outer walls of the cross-section for a short time.

Figure 6 shows the velocity contours for different cross-sections downstream of the bend considering a Dean number *De*=40000. It appears that moving away from the downstream, the fluid in the central region of the pipe moves towards the outer wall due to the centrifugal force (see Figure 6(a)). The position of the flow shows that the greatest axial velocity changes are seen by going towards the outer wall however in the case of the bend pipe with ribs, near the top and bottom walls of the pipe, the fluid moves more slowly than that near the central plane due to the presence of ribs where the flow is more accelerated pushes the fluid in the boundary layer towards the walls (see Figure 6(b)), this, therefore, requires a smaller pressure gradient to balance the centrifugal force.

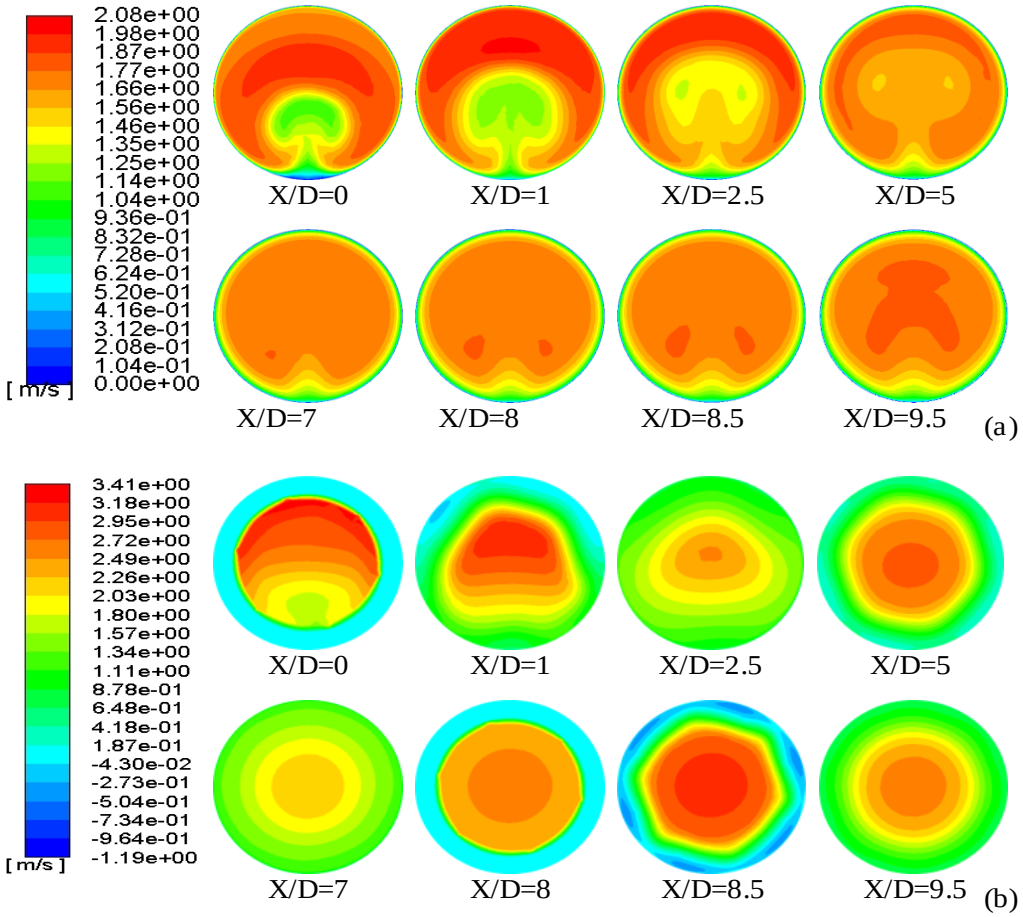

Figure 6. Streamwise velocity contours for *De*=40000 at different sections downstream of the bend. (a) bend pipe without ribs, (b) bend pipe with ribs

Anisotropy of Turbulence

The anisotropy of unsteady turbulent flows is probably the most important characteristic of the turbulence to be parameterized. The precise numerical simulation of these flows then requires to correctly predict the quantity and type of anisotropy. To do this, we exploit the properties of the Reynolds stress anisotropy tensor a_{ij}. Analysis of the characteristics of this tensor provides a good indication of the anisotropic aspect of the flow and a useful tool in the study of departures from isotropy. The second and third mathematical invariants of the Reynolds stress anisotropy tensor represented with the Lumley triangle [43] describe together the realizable states of turbulence, characterized by the positivity of the normal stresses, in any orientation.

To investigate the anisotropic behavior, we compare in this current section the anisotropy tensor invariant in Lumley's plan directly downstream the bend considering firstly the evolution of anisotropy invariant map in various positions with Dean number equal to 40000 as shown in Figure 7 and secondly we fix the position at X/D=8.5 and we vary the Dean number between 5000 and 40000 as shown in the Figure 8. This allows us to see the relationship between the transverse position and the Dean number with the distribution of the turbulence while considering the geometry with and without ribs.

Analyzing the Figure 7, it is observed just downstream the bend, that some points show a heigh level of anisotropy and does not approach to any particular spatial distribution but some points approach to the cigar-shaped limit.

By moving away from the bend Figure 7(a), we can clearly see a tendency of the invariants to approach the asymptotic branch characteristic of the axisymmetric cigar-shaped turbulence where a similar anisotropic behavior can be observed. The most anisotropic point max (*III*,-*II*)=(0.0191,0.1464) obtained in this case is located at r/R=0.997.

Figure 7(b) indicate that in the presence of ribs, the level of anisotropy decrease. Far from the ribs, the turbulence would thus be rather characterized by cigar-shaped axisymmetry, whereas downstream of the ribs near the wall and at a distance of X=1D and X=8.5D some points come close to the two-component turbulence and the Reynolds stress tensor is most anisotropic at r/R=0.8 with a maximum of (*III*,-*II*)= (0.0148,0.1238). However in all other measurement positions, the maximum value of (*III*,-*II*) occurs at r/R =0.997. Note that the peak value of *III* and -*II* is 0.0145 and 0.1183 respectively.

By inspection of the anisotropy invariant maps (AIM) represented in Figure 8(a,b), we note that the evolution of the anisotropy is practically identical, always showing a trend towards the cigar-shaped axisymmetry state with some points

that come closer to the state two-component turbulence in the case of the bend with ribs. It appears also, that the variation of the Dean number does not have a clear influence on the evolution of the anisotropy whether with or without ribs.

In conclusion, for both cases (with and without ribs), it appears that near the centerline of the pipe, the turbulence seems more isotropic (*II*=*III*=0), but it is most anisotropic near the wall at r/R=0.997 in the case of bend without ribs and at r/R=0.8 for the case of bend with ribs. However, some differences between them can still be observed, such as the increasing level and the nature of anisotropy. For this, the results show that the turbulence in the absence of ribs is more anisotropic than in the case with ribs. In fact, it occurs that in the presence of ribs the degree of anisotropy decreases by 19% and the turbulence changes its state as it has been shown in Figure 7 where it has been observed, that downstream of the ribs, some points evolve from the cigar-shaped turbulence towards the two-component turbulence.

In general, it can be seen that the analyzed flow in the bend pipe without ribs appears more anisotropic than in bend pipe with ribs. We noted an accordance between our predictions and those obtained by Shafi and Antonia [63] where they demonstrated that rough-wall turbulence appears more isotropic than its smooth-wall.

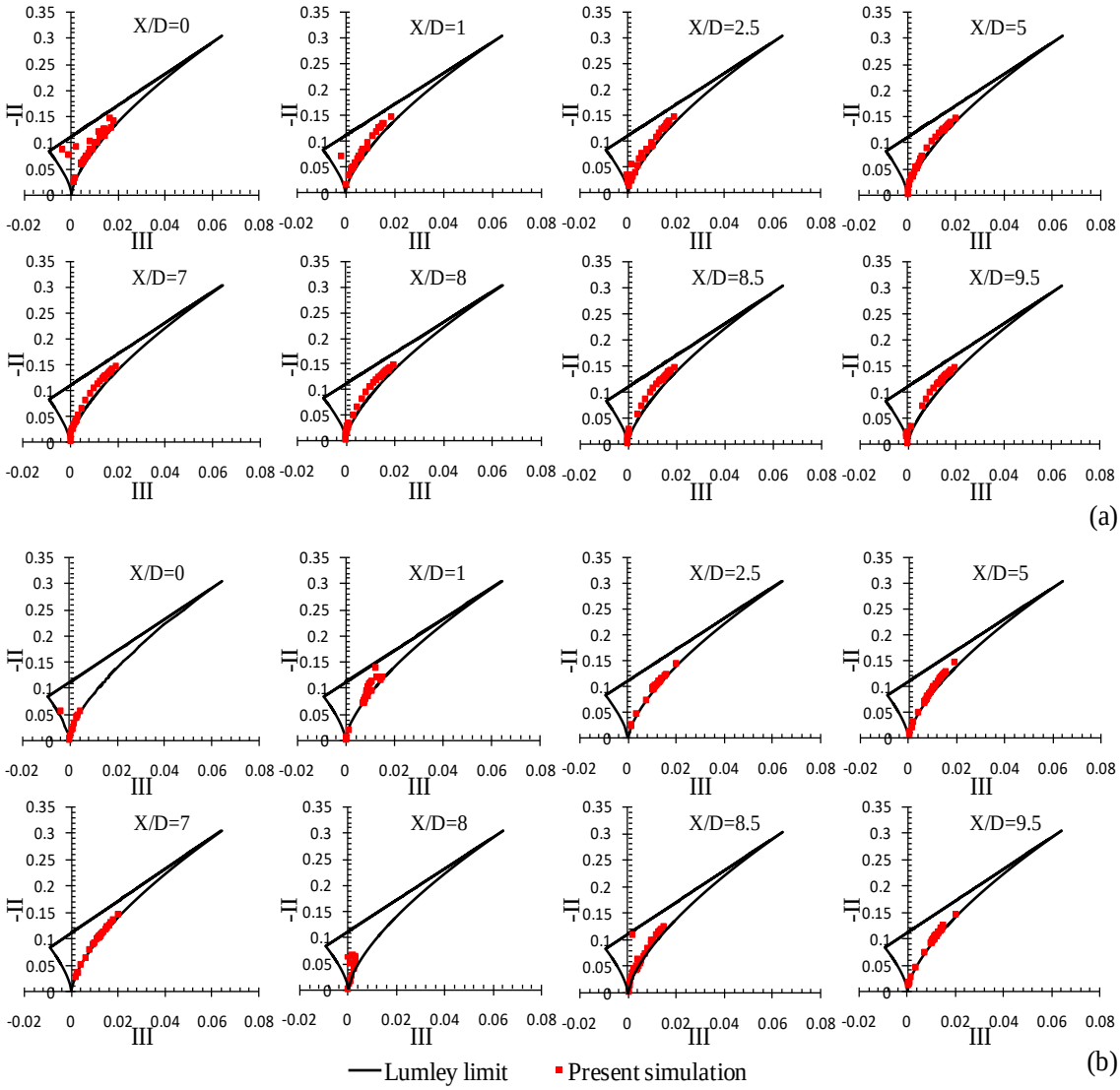

Figure 7. Distribution of the anisotropy invariants throughout the selected locations downstream the bend, *De*=40000, (a) non-ribbed bend pipe, (b) ribbed bend pipe

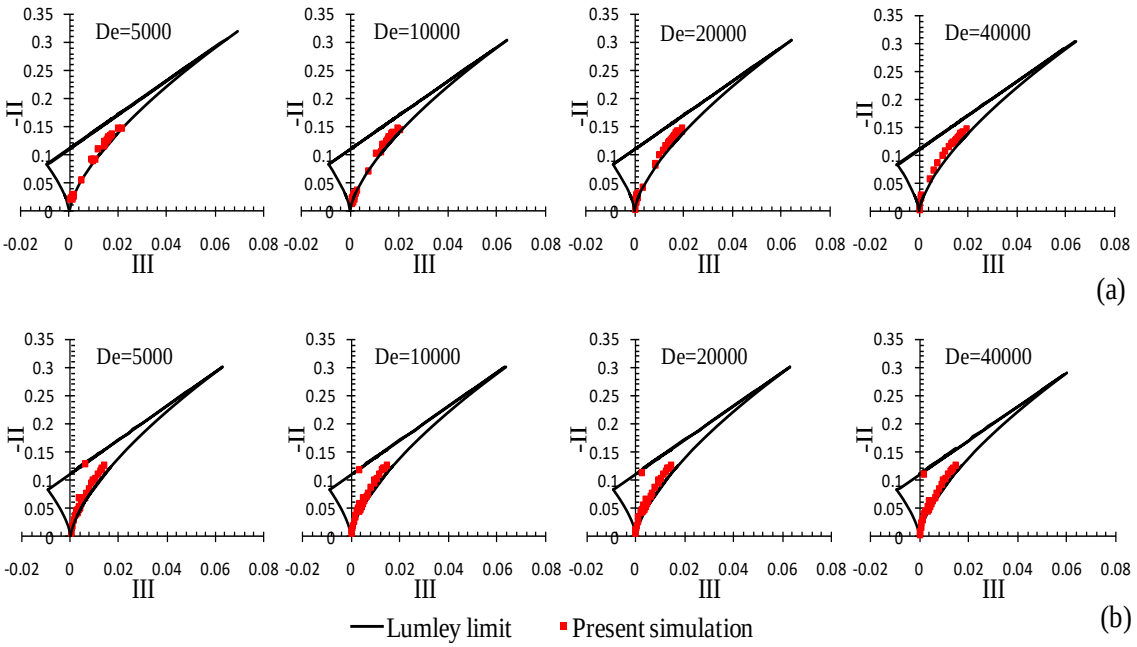

Figure 8. Distribution of the anisotropy invariants at X/D=8.5 downstream the bend for Dean number range from 5000 to 40000, (a) non-ribbed bend pipe, (b) ribbed bend pipe

Measures of Anisotropy

Figure 9, represents the anisotropy function *J* used as a measure of departure from isotropic and two-component turbulence in different positions downstream the bend for *De*=40000. From this figure, we can clearly see, that just downstream the bend with ribs (X/D=0) up to X/D=1, the turbulence in the center of the pipe (r/R=0) appears more isotropic with *J*=0.98 that in the case of bend without ribs where *J*=0.8. Although from X/D=2.5, it appears at the centerline of the bend without ribs, that the turbulence is near-isotropy compared to bend with ribs.

From X/D=0 up to X/D=5 and moving away from the center of the pipe where the turbulence is initially isotropic, it occurs that the function *J* decreases and the return to anisotropy begins to be efficient for both bend pipes considered. From X/D=7 and considering the case of the bend without ribs, an almost constant range of *J* appears in the region $0.4<r/R\leq0.7$ indicating that the distance from isotropy turbulence is smaller. However in the case of the bend with ribs, a continuous decrease in *J* is observed always showing a tendency of the flow towards anisotropy where the distance from isotropy is bigger.

Approaching the wall and taking into account the case without ribs, it appears that the function *J* gradually increases again over a short distance from r/R=0.6 up to r/R=0.8 then rapidly decreases in the region $0.8<r/R\leq1$. However, in the case of the bend with ribs, it is observed that the function *J* increases from r/R=0.6 at the level of ribs (X/D=0 and X/D=8) and from r/R=0.8 elsewhere then decreases again. Also, it must be mentioned that, behind the ribs at X/D=1 and X/D=8.5, *J* decreases and tends towards 0 showing a smaller measure of departure from a two-component state where the two-component upper boundary of the triangle ($9II+27III+1=0$) is closely satisfied by the near-wall data.

Finally, for the analyzed turbulent flow, the function *J* near the wall was smaller in the bend without ribs when compared to the bend with ribs which is in accordance with Antonia et al. [64] and Smalley et al. [65].

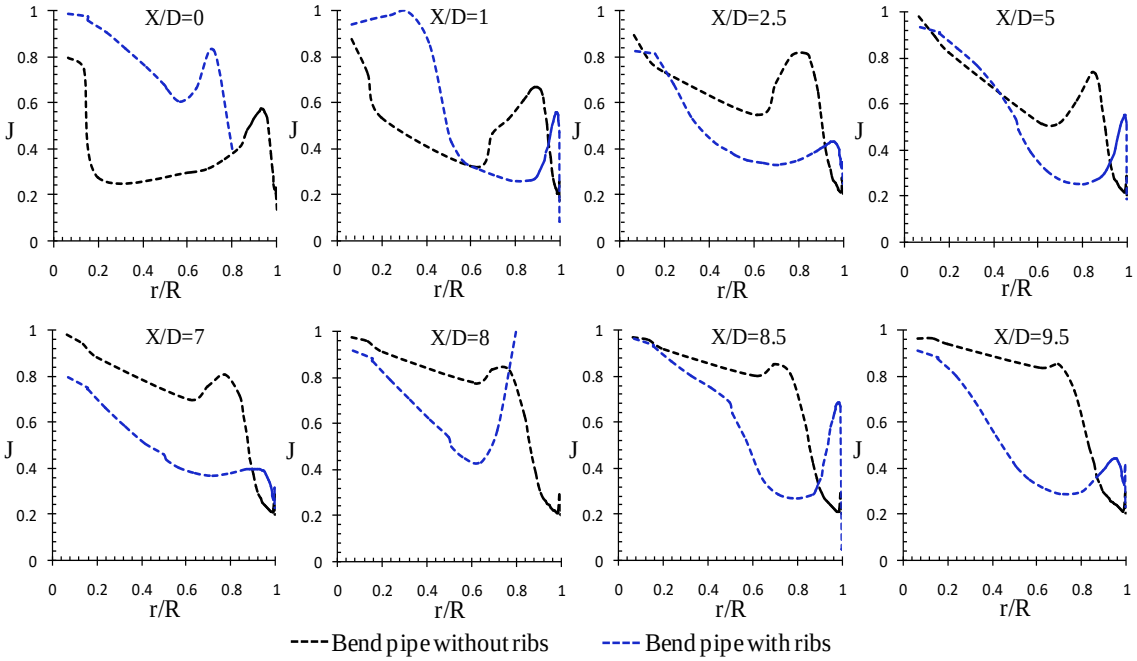

Figure 9. Comparison of the anisotropy invariant function of the turbulence throughout the selected locations downstream the bend, *De*=40000, (a) non-ribbed bend pipe, (b) ribbed bend pipe

Considering the comparison of the evolution of the function *J* at X/D=8.5 downstream of the bend exit for different Dean numbers as shown in Figure 10. It is envisaged that the maximum value of *J* is located near the centerline of the pipe (r/R=0) indicating that the turbulence in this zone is nearly isotropic where in the bend without ribs Figure 10(a), *J*=0.83, 0.89, 0.96 and 0.97 for De =5000, 10000, 20000 and 40000 respectively. It occurs, that the value of *J* for the higher Dean number to be somewhat bigger. It seems to be an effect of the Dean number. Although in the bend with ribs Figure 10(b), it appears that *J*=0.96 for different Dean numbers considered and the function *J* follows the same general trend towards the wall where a superposition of the curves representing the variation of *J* is observed showing that in the presence of ribs, the Dean number is found as a weak function.

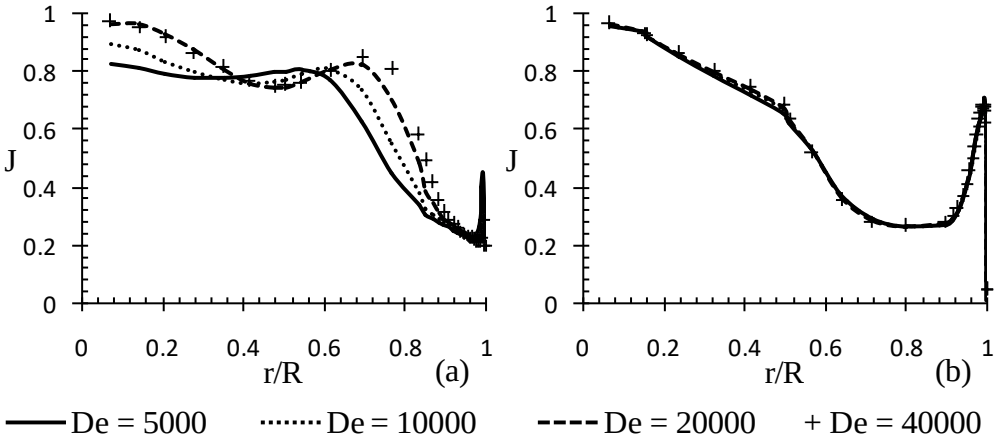

Figure 10. Comparison of the anisotropy invariant function of the turbulence at X/D=8.5 downstream the bend for Dean number range from 5000 to 40000, (a) non-ribbed bend pipe, (b) ribbed bend pipe

CONCLUSION

In the present study, a numerical simulation of the three dimensional unsteady and anisotropic turbulent flow of single-phase incompressible fluid through two 90˚bend pipes one without ribs and the other with ribs were carried in ANSYS Fluent solver using realizable RSM turbulence model. The RSM turbulence model is used in order to predict the anisotropic turbulent structure precisely. A large Dean number range from 5000 to 40000 was tested for each geometry in order to investigate its effect on flow characteristics.

For both bend pipe cases (with and without ribs) considered, the process of formation of different profiles representing the dynamic and turbulent characteristics of the analyzed flow, in the straight section, downstream the bend, was taken into consideration.

A comparison of numerical simulation results between the two geometries considered has been presented in order, to see on the one hand how the analyzed flow behaves dynamically in 90° bend pipes and on the other hand globally evaluate the impact of ribs on the velocity, anisotropy of the Reynolds stresses and anisotropy invariant function.

The conclusions based on the analysis of obtained results are presented as follows:

- Near the bend, it was observed for both cases with and without ribs that the maximum value of the U_x/u_{in} is located near the outer wall. However as it moved away from the curvature it was found that the maximum is located more towards the centerline in the bend pipe with ribs that in the case without ribs. It can be clearly noted that the profile of U_x/u_{in} in the ribbed case does not resemble the profile of the non-ribbed case, emphasizing the fact that the core flow is affected by the presence of the ribs. As a result, the higher resistance generated by the ribs produced relatively larger velocity gradient ($\partial U/\partial y$) compared to the case of bend pipe without ribs where a more uniform mean velocity profile is observed.
- The anisotropy invariants technique proposed by Lumley and Newman [43] was applied to characterize the turbulent structures of the analyzed flow. Analysis of the maps of the second and third invariants in Lumley's triangle shows that without corrective functions, the RSM model successfully restores the anisotropic character of the analyzed flow where the profiles of the second invariant as a function of the third invariant of this model are located within the admissible range of anisotropy. The maps of the second and third invariants in the Lumley plane show that the levels of anisotropy obtained with the RSM model are well predicted. This last has a greater potential to give accurate predictions for complex flows. It was also observed, that in the bend pipe without ribs a majority of points in the anisotropy invariant map is concentrated near the axisymmetric cigar-shaped turbulence whereas, in the case of ribbed bend pipe, a similar anisotropic behavior can be observed, however, some points are close to the cigar-shaped limit which shows a trend to the two-component turbulence due to the presence of ribs.
- The turbulence distributions of the analyzed flow in both considered configurations show that the influence of the Dean number on the evolution of anisotropy is not significant. While in the presence of ribs examined in this study, the magnitude of the anisotropy decreases and the flow anisotropy is modified in some points.
- Finally, for the analyzed turbulent flow, it is envisaged that at the centerline of the bend without ribs, the turbulence is near-isotropy compared to bend with ribs. However, approaching the wall, the anisotropy function appears smaller in the bend without ribs when compared to the bend with ribs where the Dean number is found as a weak function.

REFERENCES

[1] S. A. Berger, L. Talbot, and L. S. Yao, "Flow in curved pipes," *Ann. Rev. Fluid Mech*., vol. 15, no. 1, pp. 461–512, 1983, doi: 10.1146/annurev.fl.15.010183.002333.

[2] A. K. Vester, R. Örlü, and P. H. Alfredsson, "Turbulent flows in curved pipes: recent advances in experiments and simulations," *Appl. Mech. Rev*., vol. 68, no. 5, pp. 1–25, 2016, doi: 10.1115/1.4034135.

[3] J. L. Lumley, "Computational modeling of turbulent flows," *Adv. App. Mech*., vol. 18, pp. 123–176, 1979, doi: 10.1016/S0065-2156(08)70266-7.

[4] H. Ito, "Friction factors for turbulent flow in curved pipes," *J. Basic Eng*., vol. 81, no. 2, pp. 123–132, 1959, doi: 10.1115/1.4008390.

[5] W. H. Lyne, "Unsteady viscous flow in a curved pipe," *J. Fluid Mech*., vol. 45, no. 1, pp. 13–31, 1971, doi: 0.1017/S0022112071002970.

[6] B. R. Munson, "Experimental results for oscillating flow in a curved pipe," *Phys. Fluids*., vol.18, no. 12, pp. 1607–1609, 1975, doi: 10.1063/1.861077.

[7] J. A. C. Humphrey, J. H. Whitelaw, and G. Yee, "Turbulent flow in a square duct with strong curvature," *J. Fluid Mech*., vol. 103, pp. 443–463, 1981, doi: 10.1017/S0022112081001419.

[8] A. M. K. P. Taylor, J. H. Whitelaw, and M. Yianneskis, "Curved ducts with strong secondary motion: velocity measurements of developing laminar and turbulent flow," *J. Fluids Eng*., vol. 104, no. 3, pp. 350–359, 1982, doi: 10.1115/1.3241850.

[9] M. M. Enayet, M. M. Gibson, A. M. K. P. Taylor, and M. Yianneskis, "Laser-Doppler measurements of laminar and turbulent flow in a pipe bend," *Int. J. Heat & Fluid Flow*., vol. 3, no. 4, pp. 213–219, 1982, doi: 10.1016/0142-727X(82)90024-8.

[10] J. Azzola, J. A. C. Humphrey, H. Iacovides, and B. E. Launder, "Developing turbulent flow in a U-bend of circular cross-section: measurement and computation," *J. Fluids Eng*., vol. 108, no. 2, pp. 214–221, 1986, doi: 10.1115/1.3242565.

[11] P. Bovendeerd, A. Steenhoven, F. Vosse, and G. Vossers, "Steady entry flow in a curved pipe," *J. Fluid Mech*., vol. 177, pp. 233–246, 1987, doi: 10.1017/S0022112087000934.

[12] M. M. Ohadi and E. M. Sparrow, "Heat transfer in a straight tube situated downstream of a bend," *Int. J. Heat Mass Transfer*., vol. 32, no. 2, pp. 201–212, 1989, doi: 10.1016/0017-9310(89)90168-3.

[13] M. M. Ohadi, E. M. Sparrow, A. Walavalkar, and A. I. Ansari, "Pressure drop characteristics for turbulent flow in a straight circular tube situated downstream of a bend," *Int. J. Heat Mass Transfer*., vol. 33, no. 4, pp. 583–591, 1990, doi: 10.1016/0017-9310(90)90157-P.

[14] W. N. Al-Rafai, Y. D. Tridimas, and N. H. Woolley, "A study of turbulent flows in pipe bends," *J. Mech. Eng. Sci*., vol. 204, pp. 399–408, 1990, doi: 10.1243/PIME_PROC_1990_204_120_02.

[15] M. Anwer and R. M. C. So, "Swirling turbulent flow through a curved pipe," *Exp. Fluids*., vol. 14, pp. 85–96, 1993, doi: 10.1007/BF00196992.

[16] W. J. Kim and V. C. Patel, "Origin and decay of longitudinal vortices in developing flow in a curved rectangular duct(data bank contribution)," *J. Fluids Eng*., vol. 116, no. 1, pp. 45–52, 1994, doi: 10.1115/1.2910240.

[17] A. Hilgenstock and R. Ernst, "Analysis of installation effects by means of computational fluid dynamics - CFD vs experiments," *Flow Meas. Instrum*., vol. 7, pp. 161–171, 1996, doi: 10.1016/S0955-5986(97)88066-1.

[18] G. Xiaofeng and B. M. Ted, "Simulations of flow in curved tubes," *Aerosol Sci Tech*., vol. 26, no. 6, pp. 485–504, 1997, doi: 10.1080/02786829708965448.

[19] S. E. Kim, D. Choudhury, and B. Patel, "Computations of complex turbulent flows using the commercial code Fluent,"*in Modeling Complex Turbulent Flows*., vol. 7, Springer, Dordrecht, 1997, pp. 259–276, doi: 10.1007/978-94-011-4724-8_15.

[20] K. Sudo, M. Sumida, and H. Hibara, "Experimental investigation on turbulent flow in a circular-sectioned 90-degree bend," *Exp. Fluids*., vol. 25, pp. 42–49, 1998, doi: 10.1007/s003480050206.

[21] U. Kumar, S. N. Singh, and V. Seshadri, "Pressure losses in rough 90° bends of different radius of curvature," in *26th National Conference on Fluid Mechanics and Fluid Power*, I.I.T., Kharagpur, 15-17 December, 1999, pp. 337–342.

[22] T. J. Hüttl and R. Friedrich, "Direct numerical simulation of turbulent flows in curved and helically coiled pipes," *Comput Fluids*., vol. 30, no. 5, pp. 591–605, 2001, doi: 10.1016/S0045-7930(01)00008-1.

[23] T. Kawamura, T. Nakao, and M. Takahashi, "Reynolds number effect on turbulence downstream from elbow pipe," *Trans. Jpn. Soc. Mech. Eng. B*., vol. 68, no. 667, pp. 645–651, 2002, doi: 10.1299/kikaib.68.645.

[24] T. H. Chang and H. S. Lee, "An experimental study on swirling flow in a 90 degree circular tube by using particle image velocimetry," *J. Vis*., vol. 6, pp. 343–352, 2003, doi: 10.1007/BF03181741.

[25] P. L. Spedding, E. Benard, and G. M. McNally, "Fluid flow through 90 degree bends," *Dev. Chem. Eng. Mineral Process*., vol. 12, no. 1-2, pp. 107–128, 2004, doi: 10.1002/apj.5500120109.

[26] J. Pruvost, J. Legrand, and P. Legentilhomme, "Numerical investigation of bend and torus flows, part I: effect of swirl motion on flow structure in U-bend," *Chem. Eng. Sci*., vol. 59, no. 16, pp. 3345–3357, 2004, doi: 10.1016/j.ces.2004.03.040.

[27] M. Raisee, H. Alemi, and H. Iacovides, "Prediction of developing turbulent flow in 90°-curved ducts using linear and non-linear low-*Re k-ε* models," *Int. J. Numer. Meth. Fluids*., vol. 51, no. 12, pp. 1379–1405, 2006, doi: 10.1002/fld.1169.

[28] N. M. Crawford, G. Cunningham, and S. W. T. Spence, "An experimental investigation into the pressure drop for turbulent flow in 90° elbow bends," *Proc Inst Mech Eng E, J Process Mech Eng*., vol. 221, no. 2, pp. 77–88, 2007, doi: 10.1243/0954408JPME84.

[29] T. Shiraishi, H. Watakabe, H. Sago, M. Konomura, A. Ymaguchi, and T. Fujii, "Resistance and fluctuating pressures of a large elbow in high Reynolds numbers," *J. Fluid Mech*., vol. 128, no. 5, pp. 1063–1073, 2006, doi: 10.1115/1.2236126.

[30] T. Shiraishi, H. Watakabe, H. Sago, and H. Yamano, "Pressure fluctuation characteristics of the short radius elbow pipe for FBR in the postcritical Reynolds regime," *J. Fluid Sci. Technol*., vol. 4, no. 2, pp. 430–441, 2009, doi: 10.1299/jfst.4.430.

[31] J. Mojtaba, C. Cathy, and P. Hassan, "Secondary flow velocity field in laminar pulsating flow through curved pipes-PIV measurements," *Proc. ASME Fluids Eng. Div. Summer Meet*., 78141, pp. 1577–1584, 2009, doi: 10.1115/FEDSM2009-78141.

[32] A. Ono, N. Kimura, H. Kamide, and A. Tobita, "Influence of elbow curvature on flow structure at elbow outlet under high Reynolds number condition," *Nucl. Eng. Des*., vol. 241, no. 11, pp. 4409–4419, 2011, doi: 10.1016/j.nucengdes.2010.09.026.

[33] A. Noorani, G. K. El Khoury, and P. Schlatter, "Evolution of turbulence characteristics from straight to curved pipes," *Int. J. Heat & Fluid Flow*., vol. 41, pp. 16–26, 2013, doi: 10.1016/j.ijheatfluidflow.2013.03.005.

[34] C. Min and Z. Zhiguo, "Numerical simulation of turbulent driven secondary flow in a 90° bend pipe," *Adv Mat Res*., vol. 765-767, pp. 514–519, 2013, doi: 10.4028/www.scientific.net/AMR.765-767.514.

[35] L. Niu and H. S. Dou, "Stability study of flow in a 90° bend based on the energy gradient theory," in *6th International Conference on Pumps and Fans with Compressors and Wind Turbines, IOP Conf. Ser: Mater. Sci. Eng*., vol. 52, no. 2, pp. 1–6, 2013, 10.1088/1757-899X/52/2/022006.

[36] L. H. O. Hellström, M. B. Zlatinov, G. Cao, and A. J. Smits, "Turbulent pipe flow downstream of a 90° bend," *J. Fluid Mech*., vol. 735, pp. 1–12, 2013, doi: 10.1017/jfm.2013.534.

[37] K. Jongtae, Y. Mohan, and K. Seungjin, "Characteristics of secondary flow induced by 90-degree elbow in turbulent pipe flow," *Eng. Appl. Comput. Fluid Mech*., vol. 8, no. 2, pp. 229–239, 2014, doi: 10.1080/19942060.2014.11015509.

[38] P. Dutta and N. Nandi, "Effect of Reynolds number and curvature ratio on single phase turbulent flow in pipe bends," *Mech. Mech. Eng*., vol. 19, no. 1, pp. 5–16, 2015.

[39] W. Yan, D. Quanlin, and W. Pengfei, "Numerical investigation on fluid flow in a 90-degree curved pipe with large curvature ratio," *Math. Probl. Eng*., vol. 2015, no. 2, pp. 1–12, 2015, doi: 10.1155/2015/548262.

[40] R. Röhrig, S. Jakirlic´, and C. Tropea, "Comparative computational study of turbulent flow in a 90° pipe elbow," *Int. J. Heat & Fluid Flow*., vol. 55, pp. 120–131, 2015, doi: 10.1016/j.ijheatfluidflow.2015.07.011.

[41] P. Dutta, S. K. Saha, N. Nandi, and N. Pal, "Numerical study on flow separation in 90° pipe bend under high Reynolds number by *k-ε* modeling," *Eng. Sci. Technol. Int J*., vol. 19, no. 2, pp. 904–910, 2016, doi: 10.1016/j.jestch.2015.12.005.

[42] Z. Wang, R. Örlü, P. Schlatter, and Y. M. Chung, "Direct numerical simulation of a turbulent 90° bend pipe flow," *Int. J. Heat & Fluid Flow*., vol. 73, pp. 199–208, 2018, doi: 10.1016/j.ijheatfluidflow.2018.08.003.

[43] J. L. Lumley and G. Newman, "The return to isotropy of homogeneous turbulence," *J. Fluid Mech*., vol. 82, no. 1, pp. 161–178, 1977, doi: 10.1017/S0022112077000585.

[44] S. Nayak, N. Kumar, S. M. A. Khader, and R. Pai, "Effect of dome size on flow dynamics in saccular aneurysms– A numerical study," *J. Mech. Eng. Sci*., vol. 14, no. 3, pp. 7181–7190, 2020, doi: 10.15282/jmes.14.3.2020.19.0564.

[45] D. Ramírez, A. R. Clemente, and E. Chica, "Design and numerical analysis of an efficient H-Darrieus vertical-axis hydrokinetic turbine," *J. Mech. Eng. Sci*., vol. 13, no. 4, pp. 6036–6058, 2019, doi: 10.15282/jmes.13.4.2019.21.0477.

[46] P. Pasymi, Y.W. Budhi, A. Irawan, and Y. Bindar, "Three dimensional cyclonic turbulent flow structures at various geometries, inlet-outlet orientations and operating conditions," *J. Mech. Eng. Sci*., vol. 12, no. 4, pp. 4300–4328, 2018, doi: 10.15282/jmes.12.4.2018.23.0369.

[47] G. Honoré, "Numerical analysis of anisotropic turbulent flows using nonlinear turbulence models," Mechanical PhD thesis, Polytechnic of Lille. 2008.

[48] B. E. Launder, "Second-moment closure: present... and future?," *Int J Heat Fluid Fl.*, vol. 10, no. 4, pp. 282–300, 1989, doi: 10.1016/0142-727X(89)90017-9.

[49] Y. G. Lai, R. M. C. So, M. Anwer, and B. C. Hwang, "Calculations of a curved pipe flow using Reynolds stress closure," *Proc. Inst. Mech. Eng. Pt. C J. Mech. Eng. Sci*., vol. 205, no. 4, pp. 231–244, 1991, doi: 10.1243/PIME_PROC_1991_205_115_02.

[50] W. J. Richard, "Modeling strategies for unsteady turbulent flows in the lower plenum of the VHTR," *Nucl. Eng. Des*., vol. 238, no. 3, pp. 482–491, 2008, doi: 10.1016/j.nucengdes.2007.02.049.

[51] L. Belhoucine, M. Deville, A. R. Elazehari, and M. O. Bensalah, "Explicit algebraic Reynolds stress model of incompressible turbulent flow in rotating square duct," *Comput Fluids*., vol. 33, no. 2, pp. 179–199, 2004, doi: 10.1016/S0045-7930(03)00055-0.

[52] F. S. Lien and M. A. Leschziner, "Assessment of turbulence-transport models including non-linear RNG eddy-viscosity formulation and second-moment closure for flow over a backward-facing step," *Comput Fluids*., vol. 23, no. 8, pp. 983–1004, 1994, doi: 10.1016/0045-7930(94)90001-9.

[53] M. M. Gibson and B. E. Launder, "Ground effects on pressure fluctuations in the atmospheric boundary layer," *J. Fluid Mech*., vol. 86, no. 3, pp. 491–511, 1978, doi: 10.1017/S0022112078001251.

[54] S. Fu, B. E. Launder, and M. A. Leschziner, "Modeling strongly swirling recirculating jet flow with Reynolds-stress transport closures," in *6th International Symposium on Turbulent Shear Flows, Toulouse, France*, 7-9 September, 1987, pp.17-6-1–17-6-6.

[55] S. Sarkar and L. Balakrishnan, "Application of a Reynolds stress turbulence model to the compressible shear layer," *AIAA Journal*., vol. 29, no. 5, pp. 743–752, 1991, doi: 10.2514/3.10649.

[56] M. R. Nematollahi and M. Nazifi, "Enhancement of heat transfer in a typical pressurized water reactor by different mixing vanes on spacer grids," *Energy Convers. Manag*., vol. 49, no. 7, pp. 1981–1988, 2008, doi: 10.1016/j.enconman.2007.12.016.

[57] A. R. Al-Obaidi, "Influence of guide vanes on the flow fields and performance of axial pump under unsteady flow conditions: Numerical study," *J. Mech. Eng. Sci*., vol. 14, no. 2, pp. 6570–6593, 2019, doi: 10.15282/jmes.14.2.2020.04.0516.

[58] H. K. Versteeg and W. Malalasekera, *An introduction to computational fluid dynamics-the finite volume method*. Harlow: Pearson Education Limited, 2007.

[59] H. M. Quamrul, "CFD Analysis of single and multiphase flow characteristics in elbow," *Sci. Res*., vol. 4, no. 4, pp. 210–214, 2012, doi: 10.4236/eng.2012.44028.

[60] A. Sherikar and P. J. Disimile, "RANS study of very high Reynolds- number plane turbulent Couette flow," *J. Mech. Eng. Sci*., vol. 14, no. 2, pp. 6663–6678, 2020, doi: 10.15282/jmes.14.2.2020.10.0522.

[61] ANSYS Meshing User's Guide, ANSYS Inc., Southpointe 2600 ANSYS Drive Canonsburg, PA 15317, 2018.

[62] K. S. Choi and J. L. Lumley, "The return to isotropy of homogenous turbulence," *J. Fluid Mech*., vol. 436, pp. 59–84, 2001, doi: 10.1017/S002211200100386X.

[63] H. S. Shafi and R. A. Antonia, "Anisotropy of the Reynolds stresses in a turbulent boundary layer on a rough wall," *Exp. Fluids*., vol. 18, pp. 213–215, 1995, doi: 10.1007/BF00230269.

[64] R. A. Antonia and P. Å. Krogstad, "Turbulence structure in boundary layers over different types of surface roughness," *Fluid Dyn. Res*., vol. 28, no. 2, pp. 139–157, 2001, doi: 10.1016/S0169-5983(00)00025-3.

[65] R. Smalley, S. Leonardi, R. Antonia, L. Djenidi, and P. Orlandi, "Reynolds stress anisotropy of turbulent rough wall layers," *Exp. Fluids*., vol. 33, pp. 31–37, 2002, doi: 10.1007/s00348-002-0466-z.